

# Chemiexcited Photodynamic Therapy Integrated in Polymeric Nanoparticles Capable of MRI Against Atherosclerosis

Dan Mu<sup>1,\*</sup>, Xin Wang<sup>1,\*</sup>, Huiting Wang<sup>1</sup>, Xuan Sun<sup>2</sup>, Qing Dai<sup>2</sup>, Pin Lv<sup>1</sup>, Renyuan Liu<sup>1</sup>, Yu Qi<sup>2</sup>, Jun Xie<sup>2</sup>, Biao Xu<sup>2,3</sup>, Bing Zhang<sup>1,4</sup>

<sup>1</sup>Department of Radiology, Affiliated Nanjing Drum Tower Hospital of Nanjing University Medical School, Nanjing, 210008, People's Republic of China; <sup>2</sup>Department of Cardiology, Affiliated Nanjing Drum Tower Hospital of Nanjing University Medical School, Nanjing, 210008, People's Republic of China; <sup>3</sup>State Key Laboratory of Pharmaceutical Biotechnology, Nanjing University, Nanjing, Jiangsu, 210023, People's Republic of China; <sup>4</sup>Institute of Brain Science, Nanjing University, Nanjing, Jiangsu, 210008, People's Republic of China

\*These authors contributed equally to this work

Correspondence: Biao Xu; Bing Zhang, Email xubiao62@nju.edu.cn; zhangbing\_nanjing@nju.edu.cn

**Background:** Photodynamic therapy (PDT) has achieved continued success in the treatment of tumors, but its progress in the treatment of atherosclerosis has been limited, mainly due to the low tissue-penetration ability of the excitation light for photosensitizers.

**Methods:** In this study, we designed a chemiexcited system producing singlet oxygen in an attempt to apply PDT for the treatment of atherosclerosis without the irradiation of external light. The system designed was polymeric nanoparticles (NPs) equipped with chemical fuel and photosensitizers, cross-linked with an Fe<sup>3+</sup>-catechol complex for stabilization and magnetic resonance imaging (MRI).

**Results:** The system (FeCNPs for short) accumulated effectively in plaques, providing persistent and enhanced T<sub>1</sub>-weighted contrast ability. FeCNPs also prevented progression of atherosclerosis via macrophage elimination, and obviously reduced plaque size and thickness revealed by T<sub>1</sub>-weighted MRI. Expression of CD68, MCP1, and TNF $\alpha$  was significantly reduced after treatment. However, low doses of FeCNPs exhibited better therapeutic efficacy than high doses. Furthermore, low-dose FeCNPs exhibited effective macrophage elimination in aortic arches and abdominal aortae, but inefficiency in the thoracic aorta, aortic hiatus, and aorta-iliac bifurcation.

**Conclusion:** This study provides the first example of a combination of MRI and chemiexcited PDT for atherosclerosis, evidencing the effectiveness of PDT and providing significant pointers for developing nanotherapy on atherosclerosis.

**Keywords:** photodynamic therapy, atherosclerosis, chemi-excited, macrophages, MRI

## Introduction

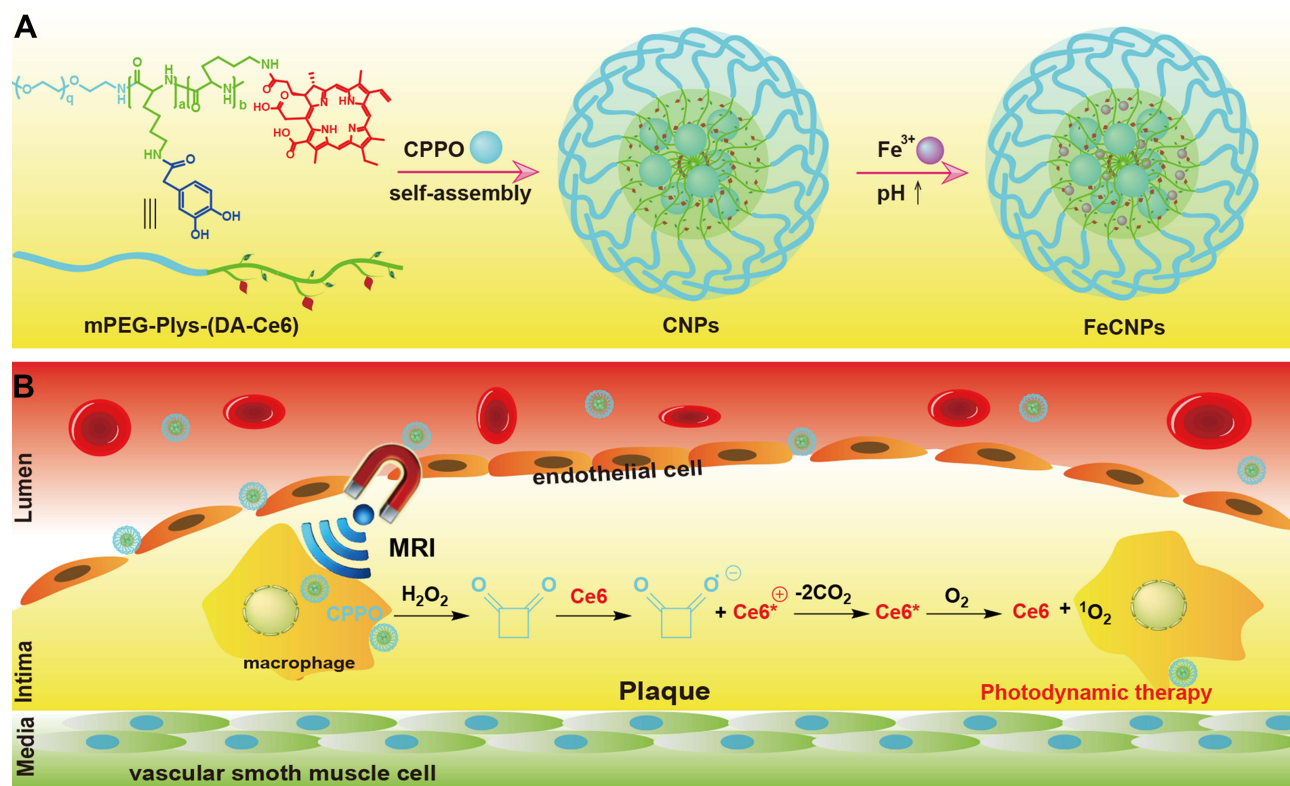
Photodynamic therapy (PDT) is an emerging noninvasive approach for tumor therapy.<sup>1-3</sup> Its functioning requires three elements: photosensitizers (PSs), light of appropriate wavelength to activate the PSs, and tissue oxygen. Due to its distinct advantages, PDT has been explored for management of atherosclerosis since last century.<sup>4,5</sup> With the development of PDT and deep understanding of atherosclerosis, positive results have been achieved, including eradicating diet-induced atheromatous plaques,<sup>6</sup> inhibiting the development of intimal hyperplasia,<sup>7</sup> and selectively eliminating macrophages.<sup>8</sup> However, negative results have also been reported.<sup>9</sup> It should be pointed out that many factors affect the evaluation of PDT in atherosclerosis, eg, types of PSs and their accumulation in plaques, the wavelength of excitation light, and experimental animal models.

Recently, different types of photodynamic nanosystems have been fabricated, including polymeric micelles or nanoparticles (NPs),<sup>10,11</sup> upconversion NPs,<sup>12,13</sup> selenium NPs,<sup>14</sup> and liposomes.<sup>15</sup> All these reports focused on the clearance of macrophages via PDT, because macrophages have evidenced its vital role in the progression of atherosclerosis.<sup>16-18</sup> However, all these studies were conducted in vitro, with none proceeding to animal models.

Caused by the strong light absorption and scattering properties of soft tissue, blood, and skin, the penetration depth of near-infrared (NIR) light is only a few millimeters, which fails to meet the requirement of the treatment of atherosclerosis.<sup>19</sup> That, we believe, is why recent trials of PDT on atherosclerosis have mostly stayed in cell experiments. Therefore, excitation light extensively restricts the application of PDT, especially in atherosclerosis.

Apart for developing new types of PSs, two approaches have been used to overcome this drawback. One is to use an optical fiber catheter inserted into the aorta to excite the PSs.<sup>20</sup> Depending on the catheter, PSs or drugs can be affixed to its surface to achieve local drug delivery. Although local administration via catheter shows greater advantages than systemic administration, it also increases the risk of infection, which may promote the progression of atherosclerosis.<sup>21</sup> The other is to use low-intensity ultrasound (stronger tissue-penetrating capability) to excite the PSs, also known as sonodynamic therapy.<sup>22</sup> Although these two approaches exhibit distinct advantages to overcome the poor penetration of light, they have deficiencies in plaque localization, which is vital to improved therapeutic efficacy and reduced side effects. Based on chemiluminescence (CL), chemiexcited PDT has been proposed, which utilizes a chemical reaction, usually between hydrogen peroxide ( $H_2O_2$ ) and a high-energy compound to excite the nearby PSs *in situ*.<sup>23</sup> Extracellular vesicles loaded with bis(2,4,5-trichloro-6-[pentylloxycarbonyl]phenyl)oxalate (CPPO), chlorin *e*<sub>6</sub> (Ce6), and the prodrug aldoxorubicin have been constructed for synergistic trimodal anticancer therapy. The reaction between  $H_2O_2$  and CPPO generates chemical energy that activates Ce6, creating both CL for imaging and singlet oxygen ( $^1O_2$ ) for PDT.<sup>24</sup> Hollow mesoporous silica NPs have been equipped with Ce6, CPPO, perfluorohexane, and glucose oxidase to develop a biomimetic nanoreactor. This biomimetic nanoreactor functioned via synergistic chemiexcited PDT and starvation therapy against tumor metastasis.<sup>25</sup> To date, no attempts have been made to develop chemiexcited PDT for atherosclerosis treatment.

In this study, monomethoxypolyethylene glycol-*block*-poly(L-lysine) modified with Ce6 and 3,4-DA (mPEG-Plys-[DA-Ce6]) was synthesized and self-assembled with CPPO. To improve stability,  $Fe^{3+}$  was introduced to coordinate with catechol groups and served as a  $T_1$ -weighted MRI contrast agent. After arrival at plaques,  $Fe^{3+}$ -catechol cross-linked CPPO-loaded mPEG-Plys-(DA-Ce6) NPs (FeCNPs) utilized the reaction between  $H_2O_2$  and CPPO to excite Ce6 for the production of  $^1O_2$  (Scheme 1). MCP1 promotes the progress of atherosclerosis via recruiting monocytes in the



**Scheme 1** Preparation (A) and functionality (B) of FeCNPs.

subendothelial cell layers, which makes it a target for atherosclerosis treatment.<sup>26</sup> It has been proved that reducing MCP1 via eliminating macrophages is a promising strategy for the treatment of atherosclerosis.<sup>27</sup> A representative proinflammatory marker, TNF $\alpha$  is also secreted by macrophages.<sup>27</sup> Therefore, MCP1, TNF $\alpha$ , and the macrophage marker CD68 were chosen to evaluate the therapeutic efficacy of FeCNPs (low and high dose) in vivo. For comprehensive evaluation, elimination of macrophages was examined in five parts of a whole aorta.

## Methods

### Materials

Monomethoxypolyethylene glycol amine (mPEG-NH<sub>2</sub>), 3,4-dihydroxyphenylacetic acid (DA), *N,N'*-dicyclohexylcarbodiimide (DCC), *N*-hydroxysuccinimide (NHS), and trifluoroacetic acid (TFA) were supplied by Shanghai Aladdin Biochemical Technology. Ce6, *N*<sup>6</sup>-carbobenzoxy-L-lysine *N*-carboxyanhydride (Lys(Z)-NCA) and 9,10-anthracenediyl-bis(methylene) dimalonic acid (ABDA) were purchased from Shanghai Maclean and Biochemical Technology. Bis(2-carboxypentyloxy-3,5,6-trichlorophenyl) oxalate (CPPO) and 33% HBr in acetic acid were bought from J&K Scientific. <sup>1</sup>O<sub>2</sub> sensor green (SOSG) and a mouse MCP1 ELISA kit were bought from Thermo Fisher Scientific. Oxidized low-density lipoprotein (oxLDL) was supplied by Shanghai Angyu Biotechnology. A hydrogen peroxide assay kit, 2-(4-amidinophenyl)-6-indolecarbamide dihydrochloride (DAPI), lipopolysaccharide (LPS), MTT cell-proliferation and cytotoxicity assay kit, and mouse TNF $\alpha$  ELISA kit were purchased from Beyotime Biotechnology. A mouse CD68 ELISA kit was purchased from MyBioSource. The antibodies were purchased from Seville Biotechnology. RAW264.7 cells were purchased from Shanghai Yiyuan Biotechnology. Organic solvent, including dichloromethane (DCM), *N,N*-dimethylformamide (DMF), and dimethyl sulfoxide (DMSO), was supplied by General Reagents and used as received.

### Synthesis of mPEG-Plys-(DA-Ce6)

#### Synthesis of mPEG-Plys(Z)

MPEG-NH<sub>2</sub> (1 g, 0.2 mmol) and Lys(Z)-NCA (0.92 g, 3 mmol) were dissolved in 15 mL anhydrous DMF. The mixture was stirred at 35°C under an N<sub>2</sub> atmosphere for 72 hours. The solvent was removed under reduced pressure. The residuals were dissolved in 10 mL DCM. The final product, mPEG-Plys(Z), was obtained by reprecipitation in ice diethyl ether.

#### Deprotection

mPEG-Plys(Z) (1 g) was dissolved in 5 mL TFA and stirred in an ice bath. HBr-acetic acid (3 mL, 33 wt%) was added slowly. After 30 minutes, the reaction was stirred at room temperature for another hour. The mPEG-Plys was isolated by precipitation into an excess amount of ice diethyl ether, further purified by dialysis against distilled water (MWCO 5,000 Da), and freeze-dried to render the pure product.

#### Conjugation of Ce6 and DA

Ce6 and DA were modified onto mPEG-Plys by condensation reaction. Briefly, Ce6 (210 mg, 0.35 mmol) and NHS (0.046 g, 0.4 mmol) were dispersed in 10 mL DMSO. DCC (0.1 g, 0.49 mmol) was added and the mixture stirred at room temperature for 4 hours. Then, the reaction mixture was added to the solution of mPEG-Plys (0.56 g, 1 mmol -NH<sub>2</sub>) in DMSO. After stirring for another 24 hours, another reaction solution containing DA (0.25 g, 1.5 mmol), NHS (0.21 g, 1.8 mmol), and DCC (0.41 g, 2 mmol) was added. The new reaction was stirred at room temperature for another 24 hours. After that, the reaction was filtrated and dialyzed against pure water for 48 hours with six changes of water.

### Preparation of Nanoparticles

Blank mPEG-Plys-(DA-Ce6) NPs (BNPs) were prepared by dialysis. In brief, 50 mg mPEG-Plys-(DA-Ce6) was dissolved in 2 mL DMSO following dialysis (MWCO 3,500) against pure water for 24 hours. The final suspension of BNPs was diluted to 1.5 mg/mL with pure water. To prepare Fe<sup>3+</sup>-catechol cross-linked NPs (FeNPs), Fe<sup>3+</sup> was mixed with BNPs (1.5 mg/mL) with a molar ratio of Fe<sup>3+</sup>:DA of 1:2. After stirring for 30 minutes, the pH of the suspension was adjusted to 7.4 with PBS (0.2 M) to make a final concentration of mPEG-Plys-(DA-Ce6) at 1 mg/mL. CPPO-loaded NPs were prepared by dialysis as well. CPPO (5 mg) and 50 mg mPEG-Plys-(DA-Ce6) were dissolved in 2 mL DMSO

following dialysis (MWCO 3,500) against pure water for 24 hours. After that, the suspension was filtered through a 0.45  $\mu\text{m}$  pore microporous membrane to obtain CPPO-loaded mPEG-Plys-(DA-Ce6) NPs (CNPs). FeCNPs were obtained by adding  $\text{Fe}^{3+}$ .

## Characterization

The chemical structure of the polymers was characterized with an NMR spectrometer (500 MHz, Bruker). Size distribution and  $\zeta$ -potential of NPs were measured by dynamic light scattering (DLS; Zetasizer Nano ZS). The morphology of NPs was investigated by transmission electron microscopy (TEM; JEM-2100). TEM samples were prepared as follows. A drop of NP suspension was placed on carbon-film copper. After staining for 5 minutes, the suspension was erased with filter paper. Then, the copper was air-dried at room temperature before measurement. The absorption spectrum of FeNPs was measured at pH 7.4 PBS by UV-vis spectroscopy (Shimadzu, UV-1280). The fluorescence spectra of Ce6, BNPs, and FeNPs with equal Ce6 content were recorded by a fluorescence spectrometer (Hitachi F-2700). The prepared sodium dodecyl sulfate (SDS) solution was mixed with the suspension of BNPs and FeNPs. The final concentrations of SDS and NPs were 3.5 and 0.5 mg/mL, respectively. Afterward, the mixture was shaken at 37°C. At predetermined time intervals, the average size of NPs was measured by DLS.

The loading capacity of CPPO in CNPs was measured. Lyophilized CNPs dissolved in DMSO were ultrafiltered (MWCO 3,000) at 9,600 g for 10 minutes. The filtrate was collected and measured by UV-vis spectroscopy. The concentration of loaded CPPO in the solution was calculated by comparison with a standard calibration curve. CPPO release from FeCNPs and CNPs was investigated in a medium of pH 7.4 with the addition of 20% methanol. FeCNPs (1 mL) or CNPs (1 mg/mL) were transferred to a dialysis bag (MWCO 2,000), which was then immersed in 40 mL medium. At predetermined intervals, the medium containing released CPPO was removed to measure the amount of CPPO and replaced by 40 mL fresh medium. All release experiments were carried out in triplicate.

## In Vitro MRI

In vitro MRI measurement of FeNPs in different concentrations at room temperature was performed with an Ingenia CX 3 T scanner (Philips Healthcare) with a human head coil. FeNPs were suspended in PBS (pH 7.4 and 6.5).  $T_1$ -weighted MR images were acquired using a turbo spin-echo sequence.  $T_1$  mapping was done using a modified Look-Locker inversion recovery (MOLLI) sequence.  $T_1$  mapping with the MOLLI sequence was calculated automatically on the MR scanner. The  $1/T_1$  relaxation time ( $\text{s}^{-1}$ ) was plotted against the Fe concentration (mM), and  $r_1$  relativity was obtained by the calculating the slope.

## Detection of Chemiluminescence

CL imaging of BNPs, FeNPs, CNPs, and FeCNPs (equal Ce6 content) with the addition of  $\text{H}_2\text{O}_2$  (1 mM) was performed and analyzed by an IVIS imaging system (PerkinElmer, XenoFluor 750).  $\text{H}_2\text{O}_2$ -dependent CL of FeCNPs was analyzed by a microplate reader (Infinite F50). Final concentrations of  $\text{H}_2\text{O}_2$  added were set at 0.1, 0.2, 0.4, 0.8, and 1.6 mM. The experiment was performed for three times.

## Detection of Singlet Oxygen

$^1\text{O}_2$  produced by FeCNPs in the presence of  $\text{H}_2\text{O}_2$  was investigated using the  $^1\text{O}_2$ -specific molecular probe ABDA. Briefly, ABDA was added into the FeCNP suspension. The final concentration of FeCNPs and ABDA was 0.5 mg/mL and 100  $\mu\text{M}$ , respectively. The mixture was divided into five equal parts in vials and incubated at 37°C in the dark.  $\text{H}_2\text{O}_2$  was added to each vial to a final concentration of 10 mM and UV-vis spectra measured every 2 minutes.

## Cell Experiments

RAW264.7 macrophages were cultured in DMEM supplemented with 10% FBS, penicillin (100 U/mL), and streptomycin (100  $\mu\text{g}/\text{mL}$ ) at 37°C with an inflow of 5%  $\text{CO}_2$ . RAW264.7 macrophages were activated by LPS (100 ng/mL) and oxLDL (40  $\mu\text{g}/\text{mL}$ ) at 37°C for 24 hours. Intracellular and extracellular  $\text{H}_2\text{O}_2$  content was measured as per the hydrogen peroxide-assay kit manual. To investigate cellular uptake, RAW264.7 macrophages were seeded in glass-bottom plates

and incubated for 12 hours. Cells were cocultured with FeNPs (0.2 mg/mL) for 1, 3, and 6 hours, then washed with PBS, fixed with 4% paraformaldehyde, and labeled with DAPI. In another experiment, cells were activated by LPS and oxLDL, cocultured with FeNPs (0.2 mg/mL) for 3 hours, then washed with PBS, fixed, and labeled. Fluorescent images of cells were photographed by a confocal laser-scanning microscope (CLSM; Leica SP5). For quantitative analysis, cells were seeded in six-well plates, activated by LPS and oxLDL, and incubated with FeNPs (0.2 mg/mL) for 3 hours, then washed with PBS, digested with trypsin, and collected in PBS before being analyzed by flow cytometry (BD FACSCalibur). The experiment was performed three times.

To verify the production of  $^1\text{O}_2$ , RAW264.7 macrophages were seeded in glass-bottom dishes, activated by LPS, and incubated with PBS, FeNPs, and FeCNPs for 6 hours. SOSG was added to the dishes to a final concentration of 5  $\mu\text{M}$ . After incubation for 1 hour, cells were washed, fixed, and photographed by CLSM. In another experiment, cells were seeded in six-well plates, activated, and incubated as aforementioned, then washed, digested, and analyzed by flow cytometry. The experiment was performed three times. The cytotoxicity of CPPO, FeNPs and FeCNPs to RAW264.7 or activated RAW264.7 macrophages was evaluated by MTT assays. Macrophages were seeded in 96-well plates at a density of 8,000 cells/well. After incubation overnight, different concentrations of FeNPs (25, 50, 100, 200, 400, and 800  $\mu\text{g/mL}$ ), CPPO or FeCNPs (1.25, 2.5, 5, 10, 20, and 40  $\mu\text{g/mL}$  CPPO) were added. In another experiment, macrophages were seeded and incubated with FeCNPs (10  $\mu\text{g/mL}$  CPPO) with or without pretreatment with  $\text{H}_2\text{O}_2$  (25, 50, 75, 100, and 125  $\mu\text{M}$ ). After 48 hour's incubation, cells were treated as per the kit manual. Optical density (OD) was recorded by a microplate reader (SpectraMax M5) at 490 nm. Cell viability was calculated:

$$\text{Cell viability \%} = \frac{OD_{\text{sample}} - OD_{\text{blank}}}{OD_{\text{control}} - OD_{\text{blank}}} \times 100 \% \quad (1)$$

where  $OD_{\text{sample}}$  represents the OD value of wells treated with different formulations,  $OD_{\text{control}}$  the OD value of wells treated with DMEM, and  $OD_{\text{blank}}$  the value of the wells with culture medium alone. The experiment was performed three times.

## Animal Experiments

Six-week old apolipoprotein E-deficient (ApoE<sup>-/-</sup>) mice were obtained from the Model Animal Research Center of Nanjing University. All animal-care and experimental protocols were carried out following review and approval from the Laboratory Animal Welfare and Ethics Committee of Nanjing University and followed the guidelines for the ethical review of laboratory animal welfare (GB/T 35892–2018). After 1 week of adaptation, mice were fed a high-fat diet for 8 weeks to establish the atherosclerosis model.

Low- or high-dose FeCNPs were injected via the tail vein at a dose equivalent to 0.5 mg/kg (n=3) or 2 mg/kg CPPO (n=3). Saline was injected as the control (n=3). After 24 or 48 hours, mice were killed and major organs and aortae collected for fluorescence imaging by the IVIS. In another experiment, mice (n=30) were randomly and equally divided into three groups: saline, low-dose (0.5 mg/kg CPPO), and high-dose (2 mg/kg CPPO) FeCNPs. The mice were intravenously injected with saline or FeCNPs twice a week for 4 weeks. Mice receiving saline served as the control group. In another experiment, mice were randomly and equally divided into two groups: saline (n=3) and 33 mg/kg FeNPs (n=3). They were intravenously injected with saline or FeNPs twice a week for 4 weeks.

After 4 weeks of treatment, the mice were killed and aortae and organs harvested. Aortae from each group were stored at  $-80^\circ\text{C}$  for measurement of the expression of CD68, MCP1, and TNF $\alpha$  as per the manuals of the ELISA kits. Aortae were fixed by paraformaldehyde (4% in PBS). After removal of the periadventitial tissue, aortae were dissected longitudinally, stained with Oil Red O (ORO), and lesions evaluated with ImageJ. Aortae fixed with 4% paraformaldehyde were paraffinized in sections. After deparaffinization, aorta sections were analyzed via H&E, Masson's trichrome, or toluidine blue staining. Expression of CD68, MCP1, and TNF $\alpha$  was also revealed via immunohistochemistry or immunostaining. Sections of organs from each group — hearts, livers, spleens, lungs, and kidneys — were also analyzed by H&E staining.

$T_1$ -weighted RARE MR images were acquired at 0, 0.5, 1, 1.5, and 2 hours from high fat-diet ApoE<sup>-/-</sup> mice injected with FeCNPs (2 mg/kg CPPO and 20  $\mu\text{mol/kg}$  Fe). Gadodiamide at the same dosage as Fe was also injected. MRI was

performed before and after treatments.  $T_1$ -weighted images were collected on a 9.4 T high magnetic field micro-MR scanner (Bruker) with a single-channel cage coil, and sequence parameters were: repetition time 800 ms, echo time 8.6 ms, flip angle  $180^\circ$ , average 8, matrix size  $300 \times 300$ , field of view  $32 \times 32 \text{ mm}^2$ , resolution  $0.107 \times 0.107 \text{ mm}$ , rare factor 2, slice number 30, slice thickness 0.5 mm, and gap thickness 0.5 mm.

## Results and Discussion

### Synthesis of Polymers

Synthesis of amphiphilic block mPEG-Plys-(DA-Ce6) copolymers was achieved with a three-step reaction (Scheme S1). Firstly, mPEG-Plys(Z) was synthesized through ring-opening polymerization of Lys(Z)-NCA in anhydrous DMF using mPEG-NH<sub>2</sub> as a macroinitiator. The degree of polymerization of mPEG-Plys(Z) was calculated to be about 11 based on the <sup>1</sup>H NMR spectrum (Figure 1A). Then, mPEG-Plys(Z) was deprotected to generate mPEG-Plys (Figure 1B). Ce6 and DA were consecutively activated using DCC-NHS and conjugated with mPEG-Plys, generating mPEG-Plys-(DA-Ce6) (Figure 1C). Upon comparison of the integral area of PEG ( $\delta=3.52$ ), DA ( $\delta=6.50$ ), and Ce6 ( $\delta=9.63$ ), the modification ratio of DA and Ce6 was calculated to be 67.5% and 28.9%, respectively. The mass ratio of Ce6 in mPEG-Plys-(DA-Ce6) was 29.9 wt%.

### Fabrication and Characterization of Nanoparticles

FeNPs showed a core-shell nanostructure (Figure 2B) with an average size of  $125.3 \pm 6.4 \text{ nm}$  (Table S1). The enhanced contrast in FeNP cores was clearly observed on TEM compared to BNPs (Figure 2A), indicating the presence of iron and formation of cross-linkage. The successful cross-linkage was responsible for the decrease in FeNP size<sup>28</sup> compared to BNPs. Cross-linkage is beneficial in that it improves the stability of NPs and resists external disturbance. As shown in Figure S1, in the presence of SDS, FeNPs exhibited better stability than BNPs. The absorption spectrum of FeNPs exhibited characteristic peaks at 405 and 660 nm, indicating successful conjugation of Ce6 (Figure 2C). It is worth noting that the absorption of FeNPs was elevated, especially in the UV region, probably due to the Fe<sup>3+</sup>-catechol complex (Figure S2). The maximum emission wavelengths of BNPs and FeNPs excited at 405 nm increased slightly compared to free Ce6, which was attributed to the chemical modification of Ce6 (Figure 2D). The fluorescence intensity of BNPs was weaker than that of free Ce6 at the same concentration, possibly due to aggregation of conjugated Ce6 driven by the self-assembly. Interestingly, the fluorescence intensity of FeNPs was further reduced, indicating the shielding effect of the Fe<sup>3+</sup>-catechol complex. Fe<sup>3+</sup>-catechol complexes in NPs and micelles have also been explored as MRI contrast agents.<sup>29,30</sup> As shown in Figure 2E, FeNPs exhibited approximate  $T_1$ -weight contrast abilities at pH 7.4 and 6.5. The longitudinal relaxivity ( $r_1$ ) of FeNPs was 4.046 mM/second at pH 7.4 and 3.820 mM/second at pH 6.5.

Because of the insolubility of CPPO in water, it was able to be encapsulated in the core of mPEG-Plys-(DA-Ce6) NPs during self-assembly. Its loading capacity in CNPs was calculated to be 7.1 wt%. The average size of CNPs increased by about 15 nm (Table S1) compared with BNPs, indicating successful CPPO loading. Interestingly, after Fe<sup>3+</sup> was introduced, reduced size of FeCNPs was still detected. CPPO release from NPs was investigated, as shown in Figure S3. Methanol (20%) was added to the release system to improve the solubility of CPPO in water, and 85.6% of CPPO was released from CNPs within 12 hours compared to 51.1% from FeCNPs, indicating enhanced stability of cross-linked NPs.

In order to verify functionality, the CL of FeCNPs was investigated (Figure 2F). Significant CL was observed in CNPs and FeCNPs. However, the CL intensity of FeCNPs was reduced at the same concentrations of Ce6, CPPO, and H<sub>2</sub>O<sub>2</sub> compared with that of CNPs. This can be explained by the wide absorption band of the Fe<sup>3+</sup>-catechol complex. The CL intensity of FeCNPs exhibited a good linear relationship ( $r^2=0.9898$ ) with the concentration of H<sub>2</sub>O<sub>2</sub> (Figure 2G). The production of <sup>1</sup>O<sub>2</sub> from FeCNPs was investigated using ABDA as an indicator. With the extension of culture time, ABDA gradually degraded, suggesting the production of <sup>1</sup>O<sub>2</sub> by CPPO-excited Ce6 (Figure 2H).

### Cytotoxicity

LPS- and oxLDL-activated RAW264.7 macrophages are often used as experimental models for atherosclerosis, because they play vital roles in the progression of atherosclerosis.<sup>31,32</sup> After activation, intracellular H<sub>2</sub>O<sub>2</sub> generation

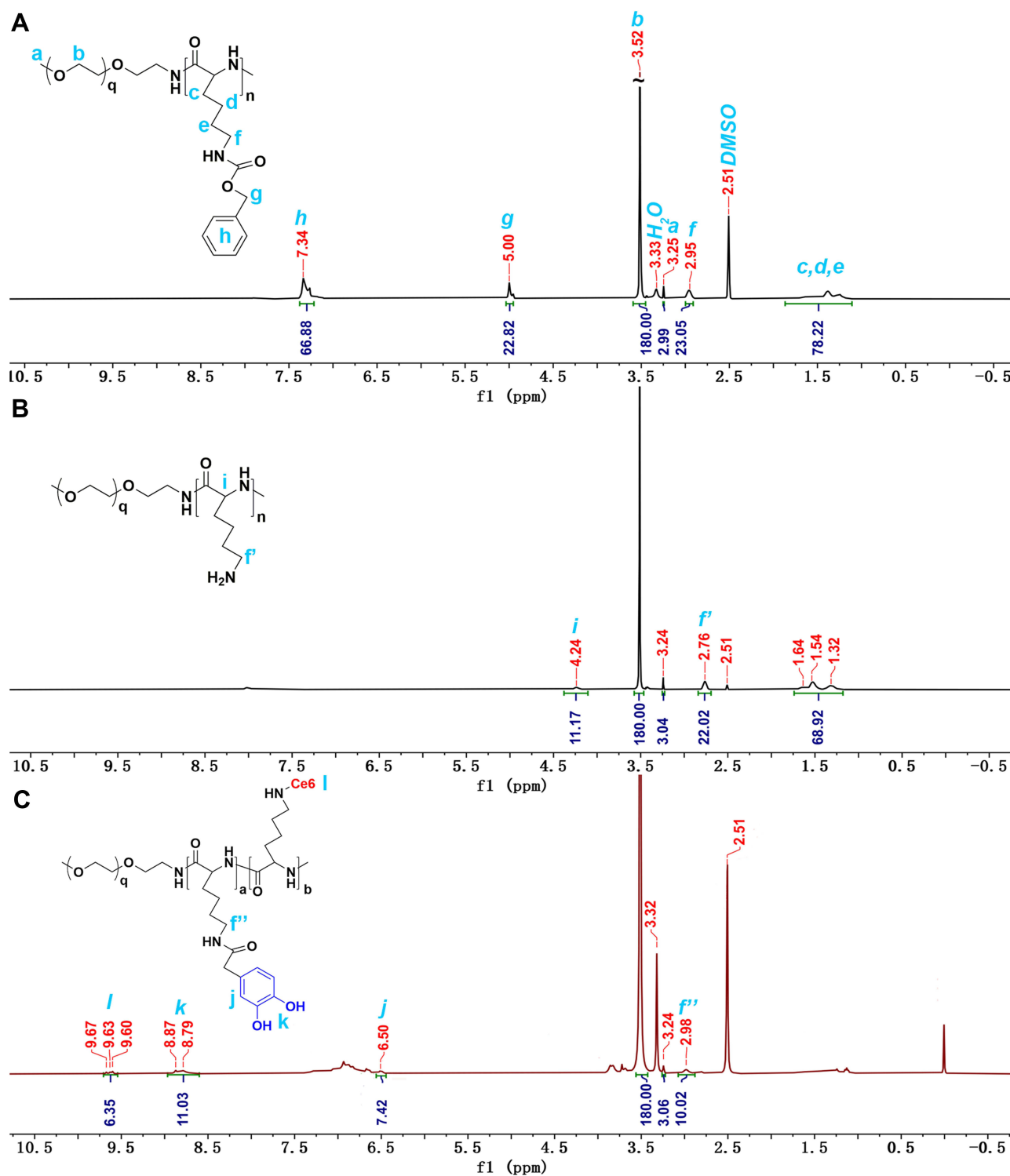


**Figure 1** <sup>1</sup>H-NMR (500 MHz) of (A) mPEG-Plys (Z), (B) mPEG-Plys, and (C) mPEG-Plys (DA-Ce6) in DMSO-*d*<sub>6</sub>.

from both cell models significantly increased (Figure S4), which was favorable for chemical excitation of PDT. Cellular uptake of FeNPs against macrophages was investigated before measuring cytotoxicity. FeNPs exhibited a time-dependent cellular uptake against RAW264.7 macrophages (Figure S5). Interestingly, LPS- and oxLDL-activated RAW264.7 macrophages internalized more FeNPs than RAW264.7 (Figure 3A and B), which could potentially increase the selectivity of PDT. After activation, the expression of some receptors was elevated, eg,

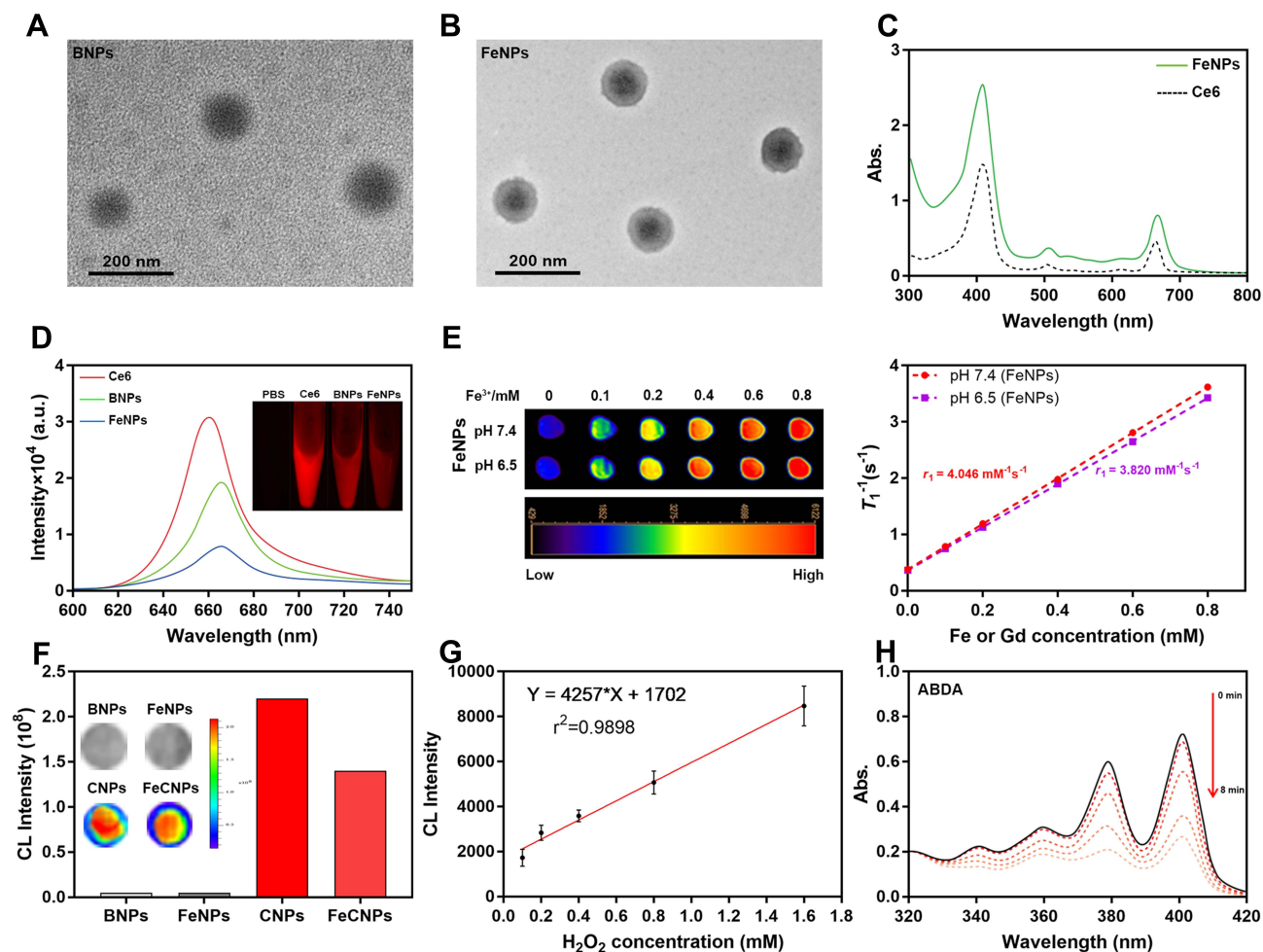


**Figure 2** Characterization of nanoparticles. Morphology of BNPs (A) and FeNPs (B). (C) Absorption spectra of Ce6 and FeNPs. (D) Emission spectra and fluorescence images of Ce6, BNPs, and FeNPs excited at 405 nm. (E)  $T_1$ -weighted MRI (left) and longitudinal plots (right) of FeNPs at various concentrations. (F) Chemiluminescence intensity of BNPs, FeNPs, CNPs and FeCNPs with  $H_2O_2$  added. Inset: chemiluminescence images. (G) Chemiluminescence intensity of FeCNPs incubated with different concentrations of  $H_2O_2$ . (H) UV-vis absorption spectra of ABDA incubated with FeCNPs and  $H_2O_2$  at different time points.

scavenger receptors,<sup>33</sup> which could explain the enhanced internalization. LPS-activated macrophages were chosen for detecting intracellular  $^1O_2$  generation using SOSG as a probe. As shown in Figure 3C and D, cells incubated with FeCNPs exhibited significant green fluorescence compared to those that had received PBS and FeNPs, indicating intracellular  $^1O_2$  produced by CPPO-excited PDT.

CPPO and FeNPs exhibited almost no cytotoxic effect against RAW264.7 cells with or without activation at the concentrations tested (Figures S6 and S7), suggesting good biocompatibility. FeCNPs exhibited dose-dependent cytotoxicity, as shown in Figure 3E. As expected, FeCNPs were more toxic to activated macrophages than macrophages without activation, mainly as a result of elevated  $H_2O_2$  production. When RAW264.7 macrophages were co-incubated with FeCNPs and different concentrations of  $H_2O_2$ , cell viability decreased dramatically (Figure 3F), evidencing  $H_2O_2$ -dependent cytotoxicity of FeCNPs.

## In Vivo Distribution

The biodistribution of FeCNPs was investigated by  $T_1$ -weighted MRI. After injection of FeCNPs, MR images of spleens, kidneys, and livers were acquired every 30 minutes, as shown in Figure S8. The signal intensity ( $S_i$ ) of organs was also measured in different areas and compared with that of precontrast images ( $S_p$ ) (Figure S9).  $S_i/S_p$  values for FeCNPs increased within 1 hour and decreased within the next hour in liver, while overall they increased in spleens and kidneys.



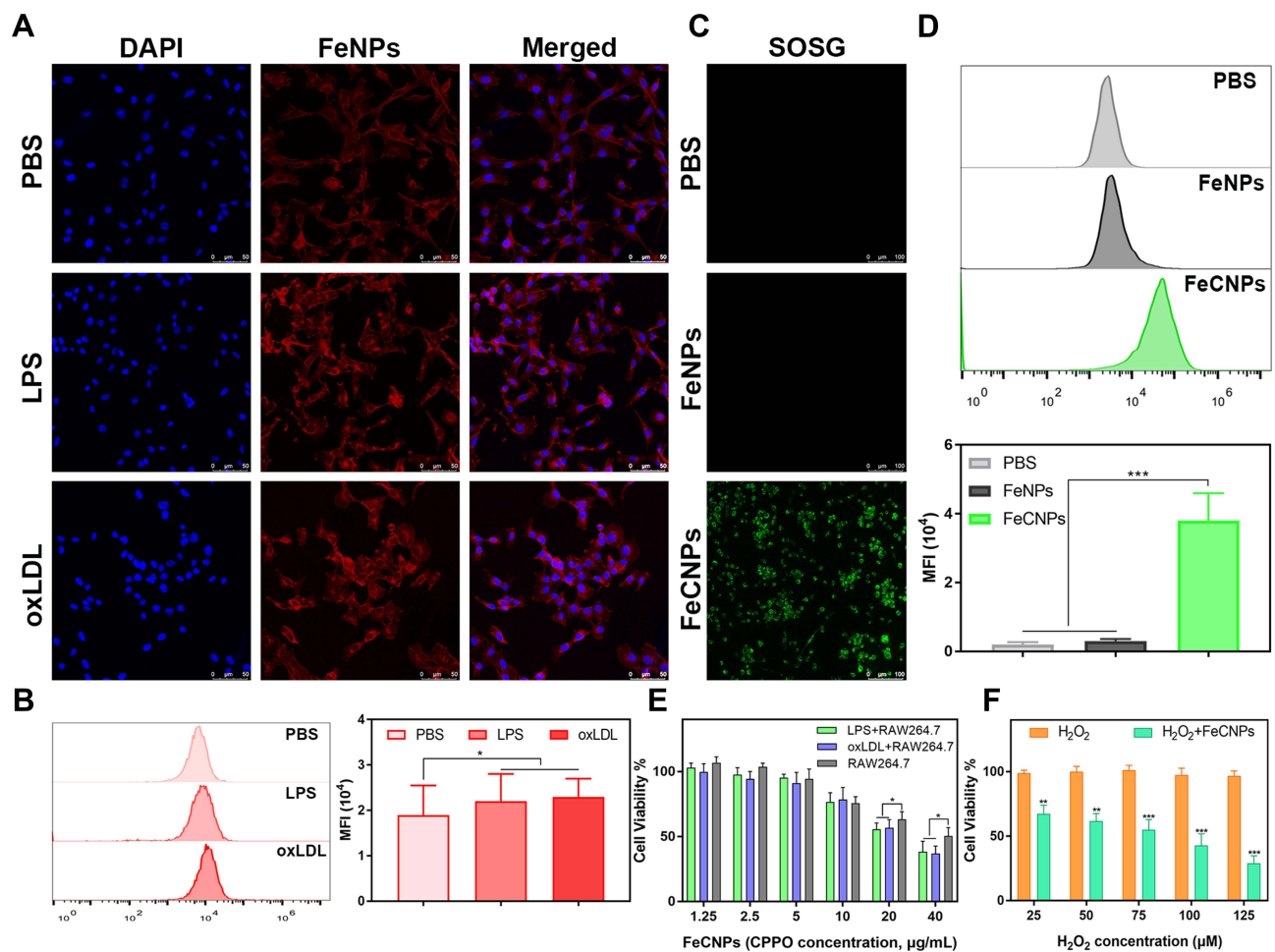


**Figure 3** (A) CLSM images and (B) quantitative analysis by flow cytometry of RAW264.7 macrophages with or without activation treated with FeNPs. The nuclei were labeled with DAPI. Bar 50 µm. SOSG fluorescence in LPS-activated RAW264.7 treated with PBS, FeNPs and FeCNPs imaged by CLSM (C) and analyzed by flow cytometry (D). Bar 100 µm. (E) Cytotoxicity of RAW264.7 with or without activation treated with FeCNPs. (F) Cytotoxicity of RAW264.7 incubated with different concentration of H<sub>2</sub>O<sub>2</sub> and then treated with FeCNPs. \**p*<0.05; \*\**p*<0.01; \*\*\**p*<0.001.

As shown in Figures 4A and S10, FeCNPs showed increasing hyperintense signals on *T*<sub>1</sub>-weighted MRI, while  $S_{\text{plaque}}/S_{\text{muscle}}$  of gadodiamide decreased gradually. Importantly, the outline of plaques was clearly observed in the magnified MR images of FeCNPs, while it was blurry in the magnified MR images of gadodiamide. The enhanced and durable contrast ability indicated effective accumulation and retention of FeCNPs in plaques. Fluorescence imaging was used to evaluate the biodistribution of low- and high-dose FeCNPs within 24 and 48 hours. As shown in Figure 4B, hearts, aortae, and livers exhibited significant fluorescence in both low- and high-dose groups compared with the control group. As expected, the fluorescence in these tissue types from the high-dose group was stronger than that from the low-dose group. Fluorescence in hearts, aortae, and livers at 48 hours had decreased obviously from 24 hours, which can be explained by elimination of NPs from the body.

## In Vivo Therapeutic Efficacy

After administration of FeCNPs twice a week for 4 weeks, plaques had decreased in both the low- and high-dose groups compared to the control group, although they were still observed on *T*<sub>1</sub>-weighted MRI (Figure S11). The maximum thickness of plaques was labeled and measured. Thickness had increased by 79.2% in the control group and 20.8% in the high-dose group and had decreased by 16% in the low-dose group. This result not only suggested great therapeutic efficacy but also proved the availability of in vivo imaging of FeCNPs.

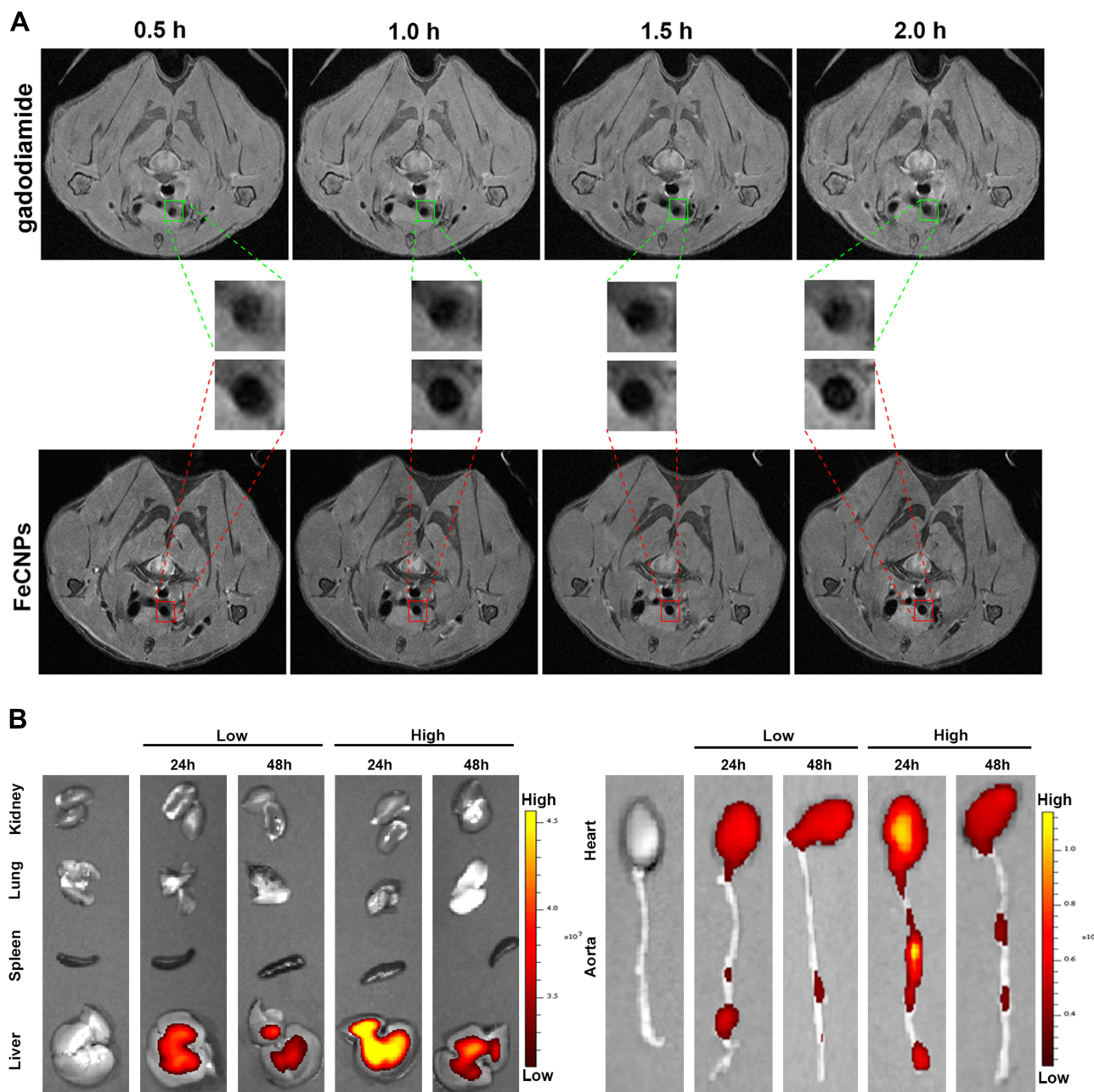


**Figure 4 (A)** T<sub>1</sub>-weighted MRI of brachiocephalic artery of high fat-diet ApoE<sup>-/-</sup> mice treated with FeCNPs and gadodiamide. **(B)** Ex vivo representative images of aortae and major organs of high fat-diet ApoE<sup>-/-</sup> mice treated with low and high dose of FeCNPs for 24 hours and 48 hours.

Entire aortae were collected and stained with ORO, as shown in Figure 5A. Relatively low ORO-stained areas in aortae were observed from mice treated with low-dose FeCNPs. However, high-dose FeCNPs did not observably reduce the ORO-stained area. ORO-positive areas were further measured (Figure 5B). Average lesion-area proportions were 66.8%, 47.5%, and 71.7% for mice treated with saline, low-dose FeCNPs, and high-dose FeCNPs, respectively. Compared with the control group, large plaques were still observed on H&E staining, while reduced necrotic cores and collagen production were observed on toluidine blue and Masson staining, respectively (Figure 5C).

MCP1 plays important roles in the progress of atherosclerosis, recruiting monocytes to migrate and accumulate in subendothelial cell layers of arteries. Then, the recruited monocytes further transform to macrophages and foam cells under the stimulation of lipids or other related factors, promoting the course of atherosclerosis.<sup>26</sup> Reducing macrophages

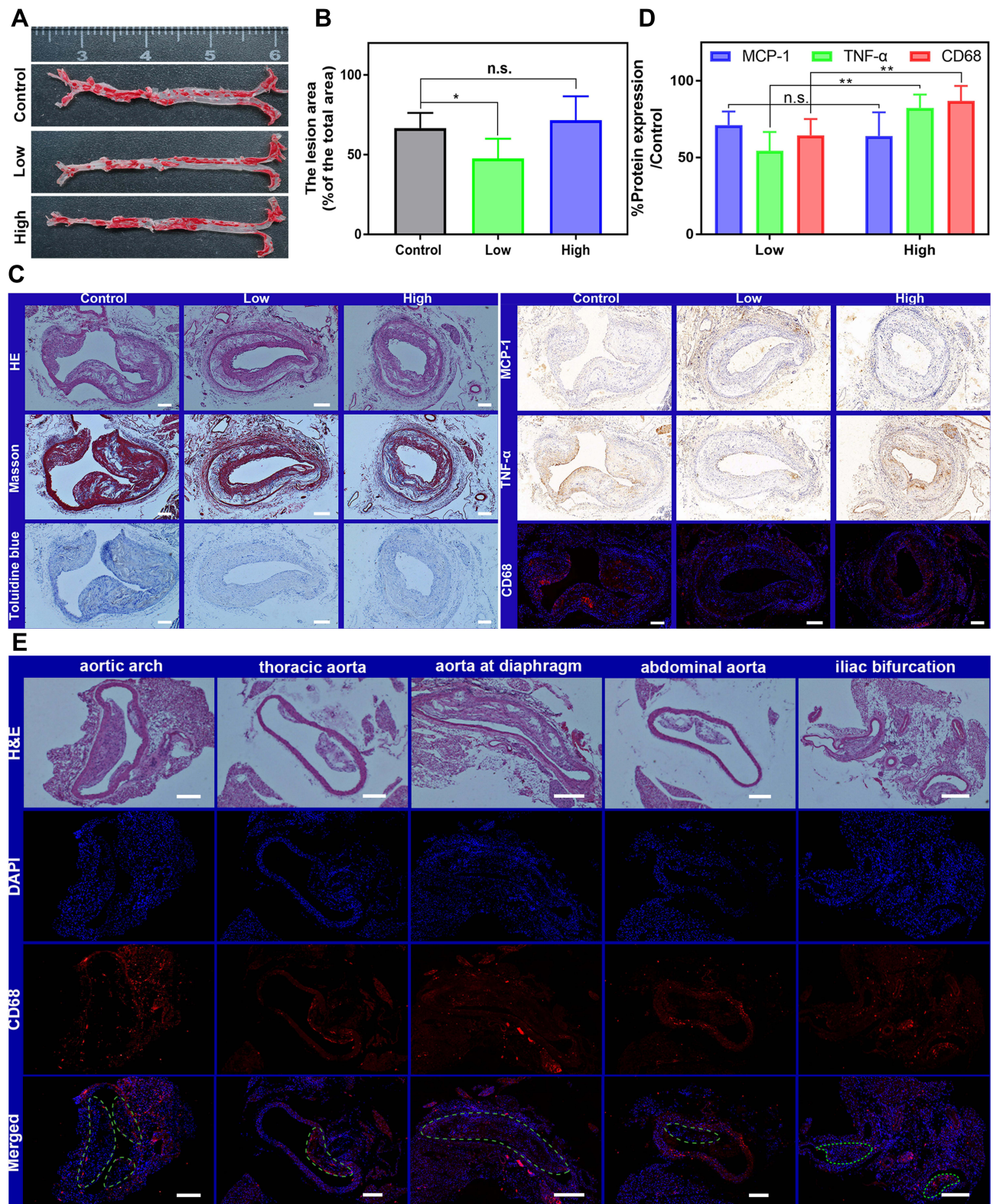


**Figure 5** (A) Representative images of ORO-stained aortae from high fat-diet ApoE<sup>-/-</sup> mice after treatment. (B) Lesion-area ratio of ORO-stained area to whole area. \* $p < 0.05$ . (C) Immunohistochemistry and immunostaining of aortic arch sections after treatment. Bar 100  $\mu$ m. (D) Quantitative analysis of expression of MCP-1, TNF $\alpha$ , and CD68. \* $p < 0.05$ ; \*\* $p < 0.01$ . (E) H&E staining and immunofluorescence staining of CD68 in five parts of the aorta from mice treated with low-dose FeCNPs. The green circle represents the region of plaques. Bar 100  $\mu$ m. **Abbreviation:** n.s., no significance.

in plaques might be an effective way to diminish the expression of MCP1. As shown in [Figure 5C](#) and [D](#), the expression of MCP1 was reduced by 28.8% and 35.9% after treatment with low- and high-dose FeCNPs, respectively. Meanwhile, the expression of TNF $\alpha$  was reduced by 45.7% (low dose) and 17.6% (high dose), and that of CD68 reduced by 35.5% (low dose) and 13.1% (high dose). Of note, low-dose FeCNPs showed better therapeutic efficacy than high-dose FeCNPs, especially in reducing TNF $\alpha$  and CD68. Though we have demonstrated a dose-dependent cytotoxicity of FeCNPs against macrophages, *in vivo* therapeutic efficacy of high-dose FeCNPs was hardly ideal. One possible reason was that the accumulation of iron in plaques accompanied by the high dose of FeCNPs exacerbated the progression of atherosclerosis. It has been reported that elevated non-transferrin bound iron aggravates atherosclerosis in mice by driving vascular dysfunction and promoting inflammation.<sup>34,35</sup> This can be partially proved by the therapeutic effect of FeNPs. As shown in [Figure S12](#), high-dose FeNPs did not change the lesion area of aortae compared to the control group, but did slightly elevate the expression of TNF $\alpha$  and CD68. Fortunately, FeCNPs did not cause significant damage to major organs ([Figure S13](#)).

These results raised our curiosity about the therapeutic effects of low-dose FeCNPs on plaques located on other parts in aortae. As shown in [Figure 5E](#), aortae from mice treated with low-dose FeCNPs were divided into five parts: aortic arch (including ascending aorta), thoracic aorta, aortic hiatus, abdominal aorta, and **aorta–iliac bifurcation**. Plaques were observed in all parts. Consistent with [Figure 5C](#), expression of CD68 in the aortic arch was reduced obviously. Reduced CD68 expression was also observed in abdominal aorta. Distinct CD68 expression was clearly detected in the thoracic aorta, abdominal aorta, and aorta–iliac bifurcation. This result indicated nonuniform therapeutic efficacy of low-dose FeCNPs. We hypothesized that the therapeutic effect was directly related to the accumulation of NPs in plaques, and the main factors affecting the accumulation of NPs may be related to the grade of plaques.<sup>36,37</sup> Therefore, modification of targeted molecules may improve the therapeutic efficacy of FeCNPs.

## Conclusion

In this study, we developed Fe<sup>3+</sup>–catechol cross-linked CPPO-loaded polymeric NPs to investigate the therapeutic efficacy of chemiexcited PDT on atherosclerosis. The therapeutic efficacy of CPPO-excited PDT was related to the degree of plaque development. Enhanced therapeutic effect may depend on improved targeting ability. In addition, the introduction of iron to nanosystems for diagnosis or therapy of atherosclerosis should be considered. The influence of iron content on the progress of atherosclerosis will be further investigated in our subsequent studies. Overall, CPPO-excited PDT is a promising and potential treatment for atherosclerosis via macrophage elimination, and plaque-targeting ability needs to be improved for better therapeutic efficacy.

## Acknowledgments

This work was supported by the National Natural Science Foundation of China (81720108022, BZ; 81601539, DM; 82070366, BX; 92068116, JX; 81870358, JX); Fundamental Research Funds for the Central Universities, Nanjing University (2020-021414380462); the Key Project of Jiangsu Commission of Health (K2019025); Social Development Project of Science and Technology Project in Jiangsu Province (BE2017707); Key Projects of Science and Technology of Jiangsu Province (BE2019602); Science Fund for Distinguished Young Scholars in Jiangsu Province; Key Medical Talents of Jiangsu Province, 13th Five-Year Health-Promotion Project of Jiangsu Province (ZDRCA2016064); Jiangsu Provincial Key Medical Discipline (Laboratory) (ZDXKA2016020); Project of the Sixth Peak of Talented People (WSN-138); Nanjing Medical Science and Technique Development Foundation (ZKX19018 and QRX17057); China Postdoctoral Science Foundation (2019M661804); Jiangsu Province Postdoctoral Science Foundation (2019k060); and New Technology Development Fund of Nanjing Drum Tower Hospital (XJSFZJJ202026).

## Disclosure

The authors report no conflicts of interest in this work.

## References

1. Wang X, Luo D, Basilion JP. Photodynamic therapy: targeting cancer biomarkers for the treatment of cancers. *Cancers*. 2021;13:2992.
2. Thakar SB, Ghorpade PN, Shaker B, Lee J, Na D. Gas-mediated cancer therapy combined with starvation therapy, ultrasound therapy, chemotherapy, radiotherapy, and photodynamic therapy: a review. *Environ Chem Lett*. 2021;19:2981–2993. doi:10.1007/s10311-021-01218-7
3. Yang H, Liu R, Xu Y, Qian L, Dai Z. Photosensitizer nanoparticles boost photodynamic therapy for pancreatic cancer treatment. *Nano-Micro Lett*. 2021;13:35. doi:10.1007/s40820-020-00561-8
4. Kossodo S, LaMuraglia GM. Clinical potential of photodynamic therapy in cardiovascular disorders. *Am J Cardiovasc Drugs*. 2001;1:15–21. doi:10.2165/00129784-200101010-00002
5. Jain M, Zellweger M, Wagnières G, van den Bergh H, Cook S, Giraud MN. Photodynamic therapy for the treatment of atherosclerotic plaque: lost in translation? *Cardiovasc Ther*. 2017;35:1–14. doi:10.1111/1755-5922.12238
6. Woodburn KW, Fan Q, Kessel D, et al. Phototherapy of cancer and atheromatous plaque with texaphyrins. *J Clin Laser Med Surg*. 1996;14:343–348. doi:10.1089/clm.1996.14.343
7. Adili F, Randolph G, Van Eps S, Flotte TJ, Lamuraglia GM. Photodynamic therapy with local photosensitizer delivery inhibits experimental intimal hyperplasia. *Lasers Surg Med*. 1998;23:263–273. doi:10.1002/(SICI)1096-9101(1998)23:5<263::AID-LSM6>3.0.CO;2-V
8. Shon SM, Choi Y, Kim JY, et al. Photodynamic therapy using a protease-mediated theranostic agent reduces cathepsin-b activity in mouse atheromata in vivo. *Arterioscler Thromb Vasc Biol*. 2013;33:1360–1365. doi:10.1161/ATVBAHA.113.301290
9. Nitta N, Seko A, Sonoda A, et al. Is the use of Fullerene in photodynamic therapy effective for atherosclerosis? *Cardiovasc Intervent Radiol*. 2008;31:359–366. doi:10.1007/s00270-007-9238-8
10. Wennink JWH, Liu Y, Mäkinen PI, et al. Macrophage selective photodynamic therapy by meta-tetra (hydroxyphenyl) chlorin loaded polymeric micelles: a possible treatment for cardiovascular diseases. *Eur J Pharm Sci*. 2017;107:112–125. doi:10.1016/j.ejps.2017.06.038
11. Yi BG, Park OK, Jeong MS, et al. In vitro photodynamic effects of scavenger receptor targeted-photoactivatable nanoagents on activated macrophages. *Int J Biol Macromol*. 2017;97:181–189. doi:10.1016/j.ijbiomac.2017.01.037
12. Han XB, Li HX, Jiang YQ, et al. Upconversion nanoparticle-mediated photodynamic therapy induces autophagy and cholesterol efflux of macrophage-derived foam cells via ROS generation. *Cell Death Dis*. 2017;8:1–11. doi:10.1038/cddis.2017.242
13. Zhu X, Wang H, Zheng L, et al. Upconversion nanoparticle-mediated photodynamic therapy induces THP-1 macrophage apoptosis via ROS bursts and activation of the mitochondrial caspase pathway. *Int J Nanomedicine*. 2015;10:3719–3736. doi:10.2147/IJN.S82162
14. Lu KY, Lin PY, Chuang EY, et al. H<sub>2</sub>O<sub>2</sub>-Depleting and O<sub>2</sub>-Generating selenium nanoparticles for fluorescence imaging and photodynamic treatment of proinflammatory-activated macrophages. *ACS Appl Mater Interfaces*. 2017;9:5158–5172. doi:10.1021/acsami.6b15515
15. Kałas W, Wysłokińska E, Przybyło M, et al. Photoactive liposomal formulation of PVP-conjugated chlorin e6 for photodynamic reduction of atherosclerotic plaque. *Int J Mol Sci*. 2019;20:3852. doi:10.3390/ijms20163852
16. Tang J, Lobatto ME, Hassing L, et al. Inhibiting macrophage proliferation suppresses atherosclerotic plaque inflammation. *Sci Adv*. 2015;1:e1400223. doi:10.1126/sciadv.1400223
17. Duivenvoorden R, Tang J, Cormode DP, et al. A statin-loaded reconstituted high-density lipoprotein nanoparticle inhibits atherosclerotic plaque inflammation. *Nat Commun*. 2014;5:1–12.
18. Gao C, Huang Q, Liu C, et al. Treatment of atherosclerosis by macrophage-biomimetic nanoparticles via targeted pharmacotherapy and sequestration of proinflammatory cytokines. *Nat Commun*. 2020;11:2622. doi:10.1038/s41467-020-16439-7
19. Liu Y, Meng X, Bu W. Upconversion-based photodynamic cancer therapy. *Coord Chem Rev*. 2019;379:82–98. doi:10.1016/j.ccr.2017.09.006
20. Jain M, Zellweger M, Aurelien F, et al. Intra-arterial drug and light delivery for photodynamic therapy using visudyne<sup>®</sup>: implication for atherosclerotic plaque treatment. *Front Physiol*. 2016;7:400. doi:10.3389/fphys.2016.00400
21. Sebastin S, Stein LK, Dhamoon MS. Infection as a cardiovascular trigger: associations between different organ system Infections and cardiovascular events. *Am J Med*. 2020;133:1437–1443. doi:10.1016/j.amjmed.2020.04.033
22. Dai T, He W, Yao C, et al. Applications of inorganic nanoparticles in the diagnosis and therapy of atherosclerosis. *Biomater Sci*. 2020;8:3784–3799. doi:10.1039/D0BM00196A
23. Mao D, Wu W, Ji S, et al. Chemiluminescence-guided cancer therapy using a chemiexcited photosensitizer. *Chem*. 2017;3:991–1007. doi:10.1016/j.chempr.2017.10.002
24. Ding J, Lu G, Nie W, et al. Self-activatable photo-extracellular vesicle for synergistic trimodal anticancer therapy. *Adv Mater*. 2021;33:2005562. doi:10.1002/adma.202005562
25. Yu Z, Zhou P, Pan W, Li N, Tang B. A biomimetic nanoreactor for synergistic chemiexcited photodynamic therapy and starvation therapy against tumor metastasis. *Nat Commun*. 2018;9:1–9. doi:10.1038/s41467-018-07197-8
26. Yin L, Peng C, Tang Y, et al. Biomimetic oral targeted delivery of bindarit for immunotherapy of atherosclerosis. *Biomater Sci*. 2020;8:3640–3648. doi:10.1039/D0BM00418A
27. Meneghini BC, Tavares ER, Guido MC, et al. Lipid core nanoparticles as vehicle for docetaxel reduces atherosclerotic lesion, inflammation, cell death and proliferation in an atherosclerosis rabbit model. *Vascul Pharmacol*. 2019;115:46–54. doi:10.1016/j.vph.2019.02.003
28. Sang X, Yang Q, Shi G, Zhang L, Wang D, Ni C. Preparation of pH/redox dual responsive polymeric micelles with enhanced stability and drug controlled release. *Mater Sci Eng C*. 2018;91:727–733. doi:10.1016/j.msec.2018.06.012
29. Xin K, Li M, Lu D, et al. Bioinspired coordination micelles integrating high stability, triggered cargo release, and magnetic resonance imaging. *ACS Appl Mater Interfaces*. 2017;9:80–91. doi:10.1021/acsami.6b09425
30. Miao Y, Xie F, Cen J, Zhou F, Tao X, Luo J. Fe<sup>3+</sup>@polyDOPA-b-polysarcosine, a T<sub>1</sub>-weighted MRI contrast agent via controlled NTA polymerization. *ACS Macro Lett*. 2018;7:693–698. doi:10.1021/acsmacrolett.8b00287
31. Darwitan A, Wong YS, Nguyen LTH, et al. Liposomal nanotherapy for treatment of atherosclerosis. *Adv Healthc Mater*. 2020;9:1–11. doi:10.1002/adhm.202000465
32. Ma B, Xu H, Zhuang W, Wang Y, Li G, Wang Y. Reactive oxygen species responsive theranostic nanoplatform for two-photon aggregation-induced emission imaging and therapy of acute and chronic inflammation. *ACS Nano*. 2020;14:5862–5873. doi:10.1021/acsnano.0c01012
33. Lian Z, Perrard XYD, Peng X, et al. Replacing saturated fat with unsaturated fat in western diet reduces foamy monocytes and atherosclerosis in male ldlr<sup>-/-</sup> mice. *Arterioscler Thromb Vasc Biol*. 2020;40:72–85. doi:10.1161/ATVBAHA.119.313078

34. Vinchi F, Porto G, Simmelbauer A, et al. Atherosclerosis is aggravated by iron overload and ameliorated by dietary and pharmacological iron restriction. *Eur Heart J*. 2020;41:2681–2695. doi:10.1093/eurheartj/ehz112
35. Iron XS. Atherosclerosis: the link revisited. *Trends Mol Med*. 2019;25:659–661. doi:10.1016/j.molmed.2019.05.012
36. Spyropoulos-Antonakakis N, Sarantopoulou E, Trohopoulos PN, et al. Selective aggregation of PAMAM dendrimer nanocarriers and PAMAM/ZnPc nanodrugs on human atheromatous carotid tissues: a photodynamic therapy for atherosclerosis. *Nanoscale Res Lett*. 2015;10:210. doi:10.1186/s11671-015-0904-5
37. Tawakol A, Castano AP, Anatelli F, et al. Photosensitizer delivery to vulnerable atherosclerotic plaque: comparison of macrophage-targeted conjugate versus free chlorine (e6). *J Biomed Opt*. 2006;11:021008. doi:10.1117/1.2186039

International Journal of Nanomedicine

Dovepress

## Publish your work in this journal

The International Journal of Nanomedicine is an international, peer-reviewed journal focusing on the application of nanotechnology in diagnostics, therapeutics, and drug delivery systems throughout the biomedical field. This journal is indexed on PubMed Central, MedLine, CAS, SciSearch®, Current Contents®/Clinical Medicine, Journal Citation Reports/Science Edition, EMBase, Scopus and the Elsevier Bibliographic databases. The manuscript management system is completely online and includes a very quick and fair peer-review system, which is all easy to use. Visit <http://www.dovepress.com/testimonials.php> to read real quotes from published authors.

Submit your manuscript here: <https://www.dovepress.com/international-journal-of-nanomedicine-journal>